Investigating the physics of higher-order optical transitions in InAs/GaSb superlattices

M. Rygała,[1] K. Ryczko,[1] T. Smołka,[1] D. Kujawa,[1] P. Martyniuk,[2,3] T. J. Ronningen,[3] S. Krishna,[3] and M. Motyka[1,*]

[1]*Department of Experimental Physics, Faculty of Fundamental Problems of Technology, Wroclaw University of Science and Technology, Wybrzeże Wyspiańskiego 27, Wrocław 50-370, Poland*

[2]*Institute of Applied Physics, Military University of Technology, ul. gen. S. Kaliskiego 2, 00-908 Warsaw, Poland*

[3]*Department of Electrical Engineering, The Ohio State University, 2024 Neil Avenue, Columbus, Ohio 43210, USA*

(Received 27 May 2021; revised 13 July 2021; accepted 23 July 2021; published 9 August 2021)

We present an optical spectroscopy analysis of the molecular beam epitaxy-grown InAs/GaSb quantum systems to study the higher-order optical transitions in InAs/GaSb superlattices (SLs). We have investigated two type-II SL structures with different layer widths: $InAs_{8ML}/GaSb_{8ML}$ and $InAs_{10ML}/GaSb_{10ML}$. To experimentally determine the spectral distribution of the higher-order transitions, the Fourier-transformed photoluminescence and Fourier-transformed photomodulated reflectance measurements were used. These measurements were undertaken vs temperature and incident polarization of the probing beam. Complementary theoretical calculations based on the eight $\mathbf{k}\cdot\mathbf{p}$ formalism were also performed to identify the electron and heavy and light hole energy band ladder. Polarization-dependent measurements indicated the interchanging nature of the light and heavy hole states for the second and third valence band vs the SL wave vector (k_z) along the growth direction. The results were compared with other calculations based on different models and existing experimental results, then summarized and reviewed for possible numerical parameters application ranges in the interface modeling.

DOI: 10.1103/PhysRevB.104.085410

I. INTRODUCTION

The midinfrared spectral range is utilized heavily in a number of important optical gas sensing applications [1], including industrial, such as the detection of hydrocarbons (e.g., methane [2], propane [3], acetylene [4], or formaldehyde [5]), and medical, such as the analysis of exhaled air [6] in the search for cancer markers [7]. Optical detection sensor systems for such applications consist of an emitter, such as a diode laser [8], quantum cascade laser [9], or interband cascade laser [10], and a detector, preferably operating at room temperature or cooled with only thermoelectric Peltier coolers. One of the devices meeting these performance requirements is a HgCdTe (MCT) detector, providing a spectral range unreachable with an indium arsenide-based detector ($>3.5\ \mu$m).

A driving force of the detector market is to provide an alternative system to MCT [11,12]. Antimonide type-II superlattices (T2SLs), such as InAs/GaSb superlattices (SLs) [13], are promising materials for both focal plane arrays and single pixel photodiodes [14] in mid- and long-wavelength infrared detection systems [15–17]. Advantages that make an InAs/GaSb T2SL a good candidate for replacing MCT are its relatively high macroscopic quantum efficiency, high absorption coefficient [13,16,18], and flexibility in the Auger recombination suppression [19].

Despite the successful development of T2SLs in recent years [17,20], there is still room for research and potential improvement since some of the physical aspects of the system are not yet fully understood. In our case, some preliminary studies of the InAs/GaSb SL system were already performed, but they were focused on midgap trap detection and their influence on the dark current of the device [21]. Moreover, different designs of T2SL-based detectors, so-called nBnN and pBnN, were compared with a common p-i-n system. Dark current density reduction in alternative designs was observed in comparison with a p-i-n device, introducing a barrier architecture allowed for the suppression of the Shockley-Read-Hall processes [22].

Experimental observations of the fundamental optical transition in InAs/GaSb have been made throughout its development, but assessments of higher-order quantum states in this system were presented only in a small number of publications. The authors were employing such methods as absorbance spectroscopy [23–27], photoluminescence spectroscopy [24,28,29], polarization sensitive photocurrent spectroscopy [30], or photomodulated reflectance spectroscopy [31]. As reliable as these results may be, they do not present clear characteristics of higher-order optical transitions. Results in Refs. [23,24] exhibited a high sensitivity for valence states, but they were limited to a certain range of GaSb thicknesses in the SL. The experiments presented in Refs. [25–28] did not have sufficient sensitivity to obtain a clear measurement of any higher-order valence states in the spectra. In Ref. [30], the authors used a method that proved to be useful for $InAs_{14ML}/GaSb_{7ML}$ SL, but any features from $InAs_{10ML}/GaSb_{10ML}$ were too weak to be observed. In Ref. [31], a photomodulated reflectance (PR) spectroscopy was used for T2SL characterization, but it was focused on the spin-orbit band measurements in the visible range. Based on our analysis of these publications, we conclude that the absorbance technique is not sensitive enough to perform a meaningful study of the higher-order valence states for

*marcin.motyka@pwr.edu.pl

InAs/GaSb SLs of equal ratio of InAs to GaSb monolayers (MLs) in the structure.

Numerical models of the InAs/GaSb SL structure were historically achieved using various calculation methods [32]. Since that time, some notable attempts were published: the empirical tight binding method [33,34], density functional theory with local density approximation [35], atomic orbital potential with general gradient approximation [36], nonequilibrium Green's function modeling [37], and two primary approaches—based on the empirical pseudopotential method [23,38–40] and the $\mathbf{k}\cdot\mathbf{p}$ theory [27,41–48].

SL systems that do not share any common atoms in their structure (such as GaAs/InP or InAs/GaSb) usually exhibit characteristic optical anisotropy which is connected to the inequivalence in the spatial arrangement of the chemical bonds appearing at the interface of the materials [49]. This effect, relating the optical properties to the polarization of the propagating light, is known as microscopic interface asymmetry (MIA), and it was proven both theoretically [50,51] and experimentally [51] for the InAs/GaSb system. To simulate this effect and its influence on the band structure, one could take a reduced symmetry approach (RSA) by modifying certain elements of the Hamiltonian used for calculations [52–54]. Alternatively, one could take an interface layer approach (ILA) and introduce thin layers of transition materials (InSb, GaAs) into the structure that simulate the chemical bonds from the structural point of view [41–55].

We present an extensive study of higher-order optical transitions with multiple experimental and theoretical approaches to the task, which resulted in the development of an energy ladder of the electron and heavy and light hole states. Polarization-dependent Fourier-transformed photomodulated reflectance (FTPR) measurements, combined with the calculations, allowed us to confirm the theory of the interchanging of the light and heavy nature of the valence states, as well as identify the number of never observed higher-order states.

II. MATERIALS AND METHODS

The samples were grown in the Oxford VG-80 using solid source molecular beam epitaxy. The details of the growth are described in other publications [56]. The epitaxial layers were grown on a Si-doped GaAs substrate. In this paper, two samples of the InAs/GaSb SL with different numbers of MLs: $\mathrm{InAs_{8ML}/GaSb_{8ML}}$ (hereafter, sample A) and $\mathrm{InAs_{10ML}/GaSb_{10ML}}$ (hereafter, sample B) were examined. Both had a total thickness $\sim 2\,\mu$m and a $\mathrm{p^+\text{-}i\text{-}n^+}$ architecture. However, to study the optical properties of the absorber, the top p-contact layer was removed using chemical etching.

A Bruker Vertex 80v spectrometer was used to measure the Fourier-transformed photoluminescence (FTPL) spectra. It operated in a step-scan mode, utilizing an external chamber for measurements with an additional modulated pump beam [57]. The PL was measured with a liquid-nitrogen cooled InSb photodiode detector. The phase sensitive detection of the optical response was performed using a lock-in amplifier. In addition to the PL, we measured FTPR spectra, which combines the advantages of modulation spectroscopy and Fourier-transform spectroscopy [58,59]. This FTPR spectroscopy has been proven sensitive to almost any optical transition occurring in the structure, including those with increased measurement difficulty. In both experiments, the pump beam was a 640 nm semiconductor laser diode, mechanically chopped at a frequency of 275 Hz.

In this paper, we consider an InAs/GaSb SL grown along the [001] direction. Assume that the InAs layer width is d_{InAs}, and the GaSb layer width is d_{GaSb}. The periodicity of an InAs/GaSb SL structure is then given by $d = d_{\mathrm{InAs}} + d_{\mathrm{GaSb}}$. The growth direction is defined as the z axis, and the x and y axes indicate [100] and [010], respectively. The energy dispersions and the corresponding wave functions of the InAs/GaSb SL in the envelope function approximation are calculated by solving the multiband Schrödinger equation:

$$\hat{H}\Psi_n(\mathbf{k}_{||}, k_z, \boldsymbol{r}) = E\Psi_n(\mathbf{k}_{||}, k_z, \boldsymbol{r}), \tag{1}$$

where $\hat{H}$ is the total eight-band Hamiltonian, Ψ is the multicomponent wave function, and E the corresponding energy. The SL wave function $\Psi_n(\mathbf{k}_{||}, k_z, \boldsymbol{r})$ can be expanded as a linear combination of the basis states $u_\nu(\boldsymbol{r})$ and the envelope function $F_n(\mathbf{k}_{||}, k_z, \boldsymbol{r})$ as follows:

$$\Psi_n(\mathbf{k}_{||}, k_z, \boldsymbol{r}) = \sum_{\nu=1}^{8} e^{i\mathbf{k}_{||}\cdot\boldsymbol{r}} u_\nu(\boldsymbol{r}) F_n(\mathbf{k}_{||}, k_z, \boldsymbol{r}), \tag{2}$$

where $\boldsymbol{r}$ is the in-plane position vector, $\mathbf{k}_{||}$ is defined as $[k_x, k_y]$, $n(\nu)$ is the subband (basis) index, k_z is the SL wave vector along the growth direction (z axis), $u_\nu(\boldsymbol{r})$ are the zone-center basis states presented in Ref. [48], $F_n(\mathbf{k}_{||}, k_z, \boldsymbol{r})$ is the υth component of the nth subband envelope function along the z axis. In the eight-band $\mathbf{k}\cdot\mathbf{p}$ approach, $F_n(\mathbf{k}_{||}, k_z, \boldsymbol{r})$ may have eight components. The total eight-band Hamiltonian is given by

$$\hat{H} = \hat{H}_{8\times 8} + \hat{H}_{\mathrm{strain}} + V(z), \tag{3}$$

where $\hat{H}_{8\times 8}$ is the operator for the kinetic energy which was described in the set of the basis states presented in Ref. [48]. Here, $\hat{H}_{\mathrm{strain}}$ describes the strain effect, and $V(z)$ describes the SL potential energy term. The explicit forms $\hat{H}_{8\times 8}$ and $\hat{H}_{\mathrm{strain}}$ Hamiltonians are given in Ref. [48].

Additionally, we used two different models describing the InAs/GaSb SL. In the RSA model, a Hamiltonian that describes the MIA effect is added [60]. Based on the theory of invariants, the authors derived the microscopic interface Hamiltonian, which in the forementioned set of basis states can be written as

$$\hat{H}_{\mathrm{RSA}} = H_{XY}\begin{bmatrix} 0 & 0 & 0 & 0 & 0 & 0 & 0 & 0 \\ 0 & 0 & 0 & 0 & 0 & 0 & 0 & 0 \\ 0 & 0 & 0 & 0 & \frac{+i}{\sqrt{3}} & 0 & 0 & -\sqrt{\frac{2}{3}} \\ 0 & 0 & 0 & 0 & 0 & \frac{+i}{\sqrt{3}} & 0 & 0 \\ 0 & 0 & \frac{-i}{\sqrt{3}} & 0 & 0 & 0 & 0 & 0 \\ 0 & 0 & 0 & \frac{-i}{\sqrt{3}} & 0 & 0 & \sqrt{\frac{2}{3}} & 0 \\ 0 & 0 & 0 & 0 & 0 & \sqrt{\frac{2}{3}} & 0 & 0 \\ 0 & 0 & -\sqrt{\frac{2}{3}} & 0 & 0 & 0 & 0 & 0 \end{bmatrix}, \tag{4}$$

where H_{XY} is an adjustable parameter characterizing the strength of the interface potential. There are two kinds of

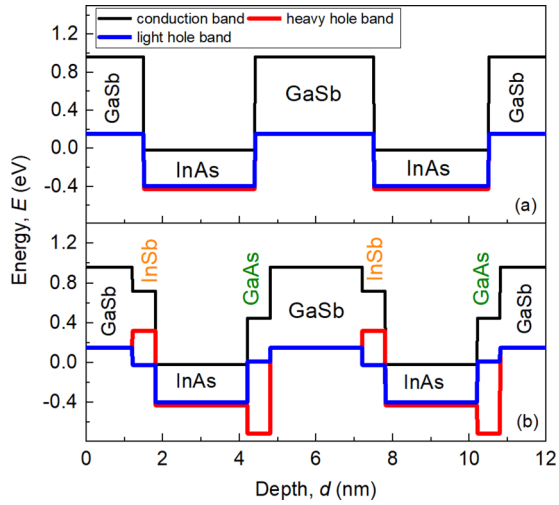

FIG. 1. Two simulated band profiles for InAs/GaSb superlattice (SL). (a) The reduced symmetry approach (RSA) profile without interface modification and (b) the interface layer approach (ILA) profile.

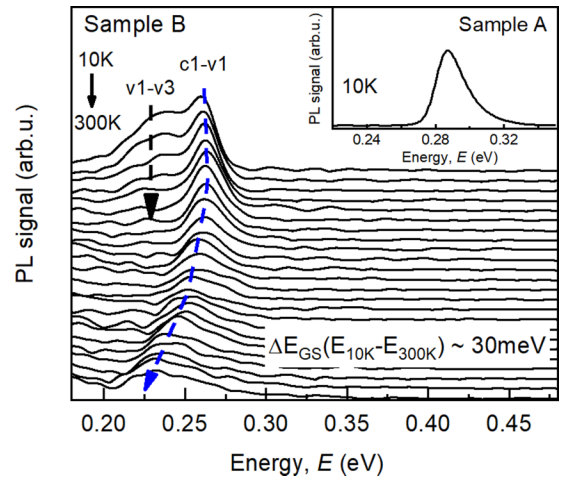

FIG. 2. Fourier-transformed photoluminescence (FTPL) signal temperature dependence for sample B. In the inset, 10 K FTPL spectrum for sample A.

interfaces in an InAs/GaSb SL: the BA interface GaSb-on-InAs at one side which can be grown InSb-like and the AB interface InAs-on-GaSb at the other side which can be grown GaAs-like [51,61]. Two additional parameters H_{XY}^{BA} and H_{XY}^{AB} characterize the strength of the InSb-like and GaAs-like interface potentials.

The second method of introducing the interface influence on the energy band, the ILA, is based on extending the potential profile by assuming additional InSb and GaAs interface bonding layers. It effectively changes the SL potential energy term.

To solve Eq. (1) numerically in real space, we use the finite difference method, knowing that the wave vector along the quantized direction is set to $k_z \rightarrow -i\partial/\partial z$. The material parameters for the 10 K temperature were taken from Ref. [62]. Knowing the calculated energies and InAs/GaSb SL energy state wave functions, we can evaluate the overlap integral for specific interband transitions, which provides the basic knowledge about the proportional oscillator strength.

Two different band structure profiles were used for numerical simulations corresponding to the two approaches for incorporating MIA. Both were created to perform the task in the framework of an eight-band $\mathbf{k}\cdot\mathbf{p}$ model, but they differed in approaching the interface problem. The RSA had a clear InAs/GaSb interface [Fig. 1(a)], while the ILA profile introduces additional thin InSb and GaAs interface layers into the structure [Fig. 1(b)]. After evaluating the numerical parameters, the optimal thickness for the InSb and GaAs interface bonding layers are equal to 0.6 nm, which is about 1 ML.

III. RESULTS

Figure 2 shows the measured FTPL signal temperature dependence for sample B. The FTPL of sample A had a similar temperature dependence, and only its 10 K spectrum is shown in the inset. In both cases, we observed PL features (marked by the blue arrow) associated with the fundamental transition between the first conduction and the first valence states ($v1$-$c1$). Low-temperature spectra for sample B also contain a weak PL feature (marked by the black arrow) which is predicted to be connected to an intersubband transition between $v3$ and $v1$ states. The PL peak energies at 10 K are close to the results calculated numerically. The 30 meV peak shift between 10 K and room temperature is typically observed for type-II band alignment systems [63]. The lack of the feature related to $v1$-$v3$ transition in PL spectrum for sample A might be due to lower signal-to-noise ratio of the photoluminescence and due to quite close coincidence of its energy with a very strong signal related to fundamental transition.

Figure 3 presents the measured FTPR spectra for InAs/GaSb SLs at 10 K. Figure 3(a) shows the PR spectrum of sample A and the closest fit (red) and marks four features predicted to be related to absorption processes between confined fundamental and excited states for either electron or hole states. Figure 3(b) shows the measured spectrum (black) for sample B and the closest fit (red).

The fitting procedure was applied for both samples and was performed with the assumption of the PR line shape according to the commonly used formula [64,65]:

$$\frac{\Delta R}{R}(E) = \mathrm{Re}\left[\sum_{j=1}^{n} C_j e^{i\theta_j}(E - E_j + i\Gamma_j)^{-m_j}\right], \qquad (5)$$

where n is the number of optical transitions and independent spectral functions used in the fitting procedure, C_j and θ_j are the amplitude and phase parameters, E_j and Γ_j are the energy and the broadening parameter of the transitions, respectively, and m_j is a parameter depending on the type of optical transition. The value of the m_j parameter for PR is equal to 3, accounting for the PR line shape for confined state transitions [66].

The other fitting parameters are not discussed, as they are not relevant for the purpose of the determination procedure of the transition intensities vs polarization of incoming light. Fitted curves are shown together with the moduli of the associated resonances (dashed blue lines) obtained according to

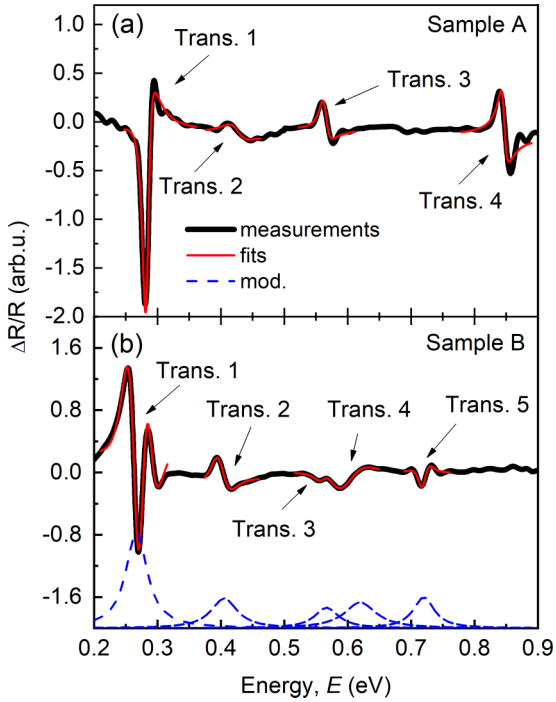

FIG. 3. Measured Fourier-transformed photomodulated reflectance (FTPR) spectra at 10 K (black curves) with optical transitions indicated with arrows for (a) sample A and (b) sample B with examples of the fit spectra (red). (b) includes the modulus (dashed blue) for sample B.

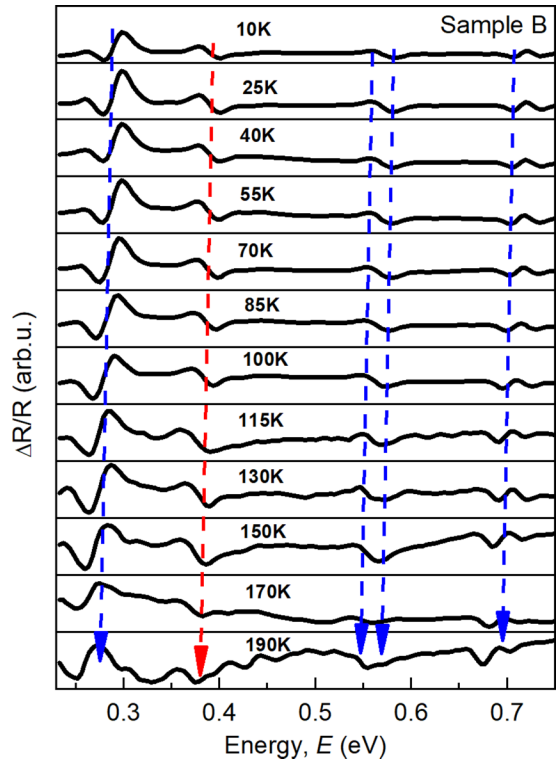

FIG. 4. Temperature-dependent Fourier-transformed photomodulated reflectance (FTPR) spectra of sample B (black) with the temperature trend of five transitions indicated with blue or red.

Eq. (6):

$$\Delta\rho(E) = \frac{|C|}{[(E - E_0)^2 + \Gamma^2]^{m/2}}. \tag{6}$$

According to the fitting results, Transition 1 corresponds to the first heavy hole states at 270 meV in sample A and at 290 meV in sample B. These are consistent with the FTPL observations at 10 K. Transitions 2–5 at higher energies are associated with higher-order electron and light and heavy hole states and are discussed further below.

To interpret Transitions 2–5, the temperature-dependent FTPR spectra were measured. Figure 4 shows the temperature dependence for sample B. For better clarification, transitions expected to originate from light and heavy hole valence bands are indicated with red and blue color, respectively.

All the energy shifts are inversely proportional to the sample temperature, which is an expected behavior related to increasing lattice constants and the corresponding InAs and GaSb band gap reduction.

Furthermore, all transition energies change with a similar rate; therefore, we conclude that all features are connected with interband transitions and none of them with intersubband transitions. Intersubband transitions, those that occur within electron or hole subbands, are expected to be nearly temperature independent [67].

Figure 5(a) shows a calculated dispersion of the energies for the electron (gray), the heavy hole (blue), and the light hole (red) bands for the RSA model and rectangular band profile. These calculated values were optimized, as described further below, to provide the best agreement with the measurements. The x axis of the figure should be understood as the number of either InAs MLs or GaSb MLs in the single well structure, as they are always equal in the material system discussed in this paper.

The FTPL and FTPR transitions are observed at the Γ point of the Brillouin zone, and they can correspond to either of the van Hove singularities—a three-dimensional minimum of the k_z vector ($k_z = 0$) or to a saddle point ($k_z = \pi/d$) [68].

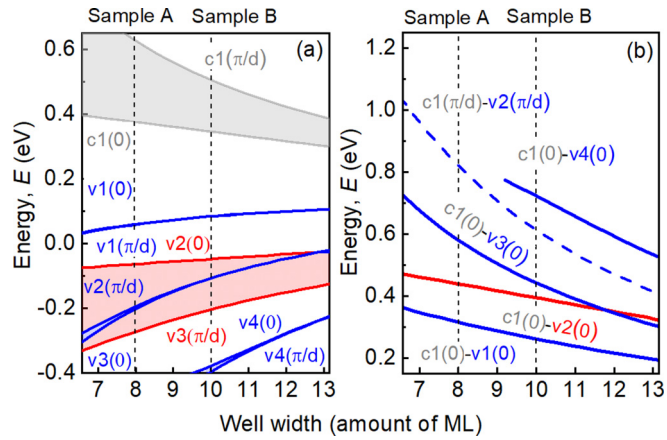

FIG. 5. (a) Calculated InAs/GaSb superlattice (SL) energy bands and (b) optical transition energies (for 0 and π/d values of the SL wave vector k_Z) from the reduced symmetry approach (RSA) model. Vertical dashed lines indicate the samples studied in this paper.

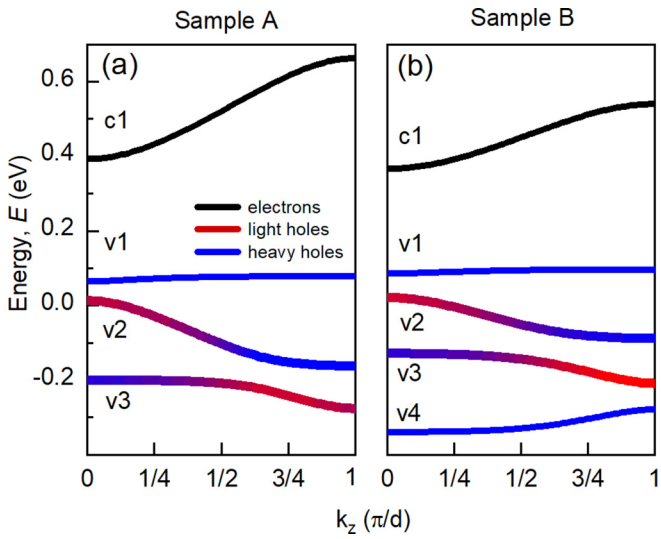

FIG. 6. Calculated energies of the confined bands along the superlattice (SL) wave vector k_Z for (a) sample A and (b) sample B. Black lines denote the electron state. For the hole states, blue denotes the heavy hole character, red denotes the light hole character, and the gradient denotes their common contribution.

Therefore, our FTPR measurements only capture the optical features occurring for the energy bands at these two boundary values of k_z.

The electron and light hole band broadening are significant in comparison with the heavy hole band broadening due to their small effective mass.

Figure 5(b) shows the calculated energies for optical transitions corresponding to the energy bands in Fig. 5(a). The graph presents all transitions with significant overlap integral between the wave functions of electrons and holes for k_Z values of 0 and π/d. These transition energies can be compared with the experimental results for samples A and B, and this comparison is discussed below.

For a better understanding of the origin of the transitions, calculated band structures for samples A and B are presented in Figs. 6(a) and 6(b), respectively. A black line represents electrons, while the blue and red colors denote heavy and light hole characters of the bands. For the $v2$ and $v3$ bands, moving across the k_z values from 0 to π/d, there is an interesting gradient between the red and blue colors indicating a transition in their hole character. Specifically, at $k_z = 0$, the $v2$ band has a light hole nature, while $v3$ has a heavy hole nature, whereas at $k_z = \pi/d$, the $v2$ and $v3$ bands have heavy hole and light hole natures, respectively. The $v1$ and $v4$ (predicted only for sample B) bands have a constant heavy hole nature for all values of k_z. This prediction of interchanging valence nature will be discussed in more detail below, after the final verification of the measurements with calculated transition energies from numerical procedures. The additionally observed $v4$ band is a result of the change in the confinement potential due to the increased thickness of the layers in sample B. This increase allows for an additional valence band to quantize inside the wells.

TABLE II. FTPR transitions observed in the system with corresponding notation.

	Energy (eV)	Valence nature	k_z value	Notation
Sample A				
Transition 1	0.292	Heavy hole	0	$v1$-$c1(0)$
Transition 2	0.412	Light hole	0	$v2$-$c1(0)$
Transition 3	0.567	Heavy hole	0	$v3$-$c1$ (0)
Transition 4	0.848	Heavy hole	π/d	$v2$-$c1(\pi/d)$
Sample B				
Transition 1	0.267	Heavy hole	0	$v1$-$c1(0)$
Transition 2	0.399	Light hole	0	$v2$-$c1(0)$
Transition 3	0.564	Heavy hole	0	$v3$-$c1$ (0)
Transition 4	0.597	Heavy hole	π/d	$v2$-$c1(\pi/d)$
Transition 5	0.719	Heavy hole	0	$v4$-$c1$ (0)

The same material parameters (Table I) were used for both the RSA and ILA approaches. Both approaches were numerically optimized to provide the best agreement with the measured transition energies observed at 10 K. A clear agreement between theory and experiment allowed us to recognize and identify the observed transitions which are presented in Table II.

Results of the RSA calculations are shown in Figs. 7(a) and 7(b), while the results of the ILA are presented in Figs. 7(c)

TABLE I. Material parameters for the calculation.

Parameter or material		Symbol (unit)	InAs	GaSb
Band gap		E_g (eV)	0.410	0.811
Spin-orbit energy		Δ (eV)	0.380	0.750
Interband matrix energy parameter		E_P (eV)	22.2	22.4
Electron effective mass		$m_e(m_o)$	0.023	0.042
Luttinger parameters		γ_1	19.67	11.40
		γ_2	8.37	4.03
		γ_3	9.29	5.26
Lattice constant		a (nm)	0.6058	0.6082
Elastic stiffness constant		$C_{11}(10^{11}\,\mathrm{dyn}\cdot\mathrm{cm}^{-2})$	8.329	8.842
		$C_{12}(10^{11}\,\mathrm{dyn}\cdot\mathrm{cm}^{-2})$	4.526	4.026
Hydrostatic deformation potential	Conduction band	a_c (eV)	−5.08	−7.50
	Valence band	a_v(eV)	−1.00	−0.80
Shear deformation potential for valence band		b (eV)	−1.80	−2.00

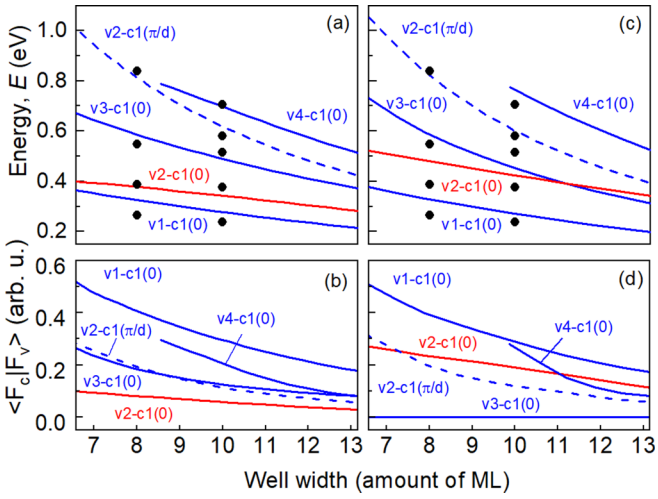

FIG. 7. (a) and (c) The calculated transition energies and (b) and (d) relative overlap integral for five optical transitions vs InAs and GaSb thicknesses for the reduced symmetry approach [RSA; left side, (a) and (b)] and interface layer approach [ILA; right side, (c) and (d)]. Observed Fourier-transformed photomodulated reflectance (FTPR) transition energies are denoted with the black points.

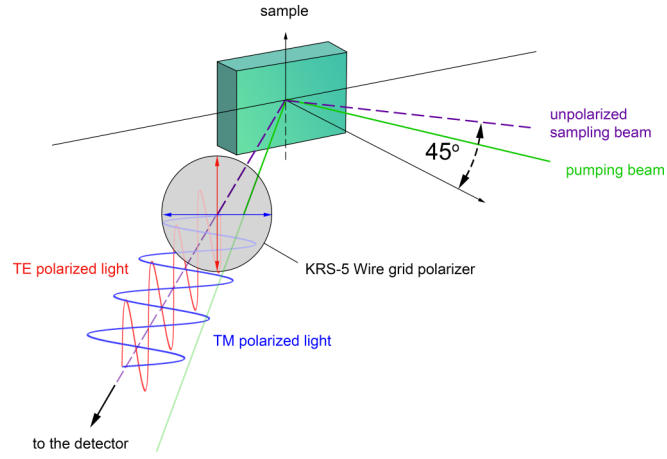

FIG. 8. Principle of the Fourier-transformed photomodulated reflectance (FTPR) experiment setup utilizing the KRS-5 wire-grid polarizer.

and 7(d). Note, in the ILA, we could not find reasonable overlap integral for $v3$-$c1(0)$ transition, and it is presented as equal to zero.

An important advantage of the calculations performed in this paper is the capability to optimize them with reference to nine directly measured transition energies, especially the $v4$-$c1(0)$ connected with the third heavy hole band (observed only for sample B). Some of the transitions at $k_z = \pi/d$, such as $v1$-$c1(\pi/d)$ and $v3$-$c1(\pi/d)$ are not considered due to their negligible oscillator strength. All reasonable transitions have their overlap integrals shown in Figs. 7(b) and 7(d).

These predictions and assignments were further evaluated against a series of polarization-dependent FTPR measurements. The FTPR experiment was modified to realize the measurements vs polarization of the reflected light, as shown in Fig. 8. A polarizing plate transmits only the reflected light with a certain linear polarization, transverse magnetic (TM) or transverse electric (TE). TM polarization denotes the oscillations in the growth direction and TE polarization the in-plane direction. Choosing the polarization of the detected spectra allows the sampling of the optical features visible only for certain oscillation planes. It further restricts the selection rules within the quantum confined systems. This type of experimental setup was successfully applied for polarization-dependent FTPR study [69].

Figure 9 shows a set of the PR spectra at 10 K obtained for different angles of the polarizing plate, and each angle corresponds to a different proportion of the TE and TM polarization in the probing light. Transitions to the heavy hole states are marked by the blue dashed line, and transitions to the light hole states are marked by a red dashed line. We see that $v1$-$c1(0)$, the fundamental transition, is fairly polarization independent, which is a result of its strong oscillator strength. The remaining transitions seem to be very sensitive to changes in the TE/TM ratio of the reflected probing light. Here, $v2$-$c1$ is weakest at 0° polarizer position and strongest ∼90°. In contrast, $v3$-$c1(0)$ and $v2$-$c1(\pi/d)$ are strongest at 0° and weakest ∼90°.

The disappearance of certain features with polarization is possible due to a their much smaller oscillator strength in comparison with the fundamental transition [see Figs. 7(b) and 7(d)]. Changing the position of the polarizer effectively

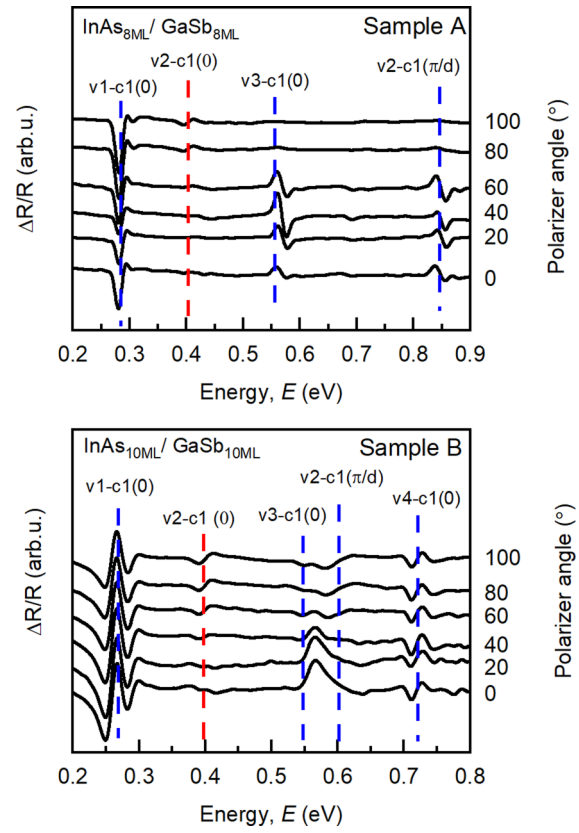

FIG. 9. The photomodulated reflectance (PR) spectra measured for different light polarization for (a) sample A and (b) sample B, respectively.

TABLE III. Comparison of the data obtained in this paper [experimental and theoretical according to Fig. 7(a)] with theoretical results predicted in literature for $InAs_{8ML}/GaSb_{8ML}$ (top) and $InAs_{10ML}/GaSb_{10ML}$ (bottom).

Optical transition (initial state to final state)	Our experimental results (eV)	Our theoretical results (eV)	Theoretical results (eV) from: [41]	[55]	[51]	[35]	[52]	[70]	[30]
Sample A									
$v1$-$c1(0)$	0.292	0.329	0.313	0.238	0.248	0.305	0.271	0.215	
$v2$-$c1(0)$	0.412	0.380	0.412	0.378	0.397	0.460	0.363	0.391	
$v3$-$c1(0)$	0.567	0.594	0.616	0.494	0.466	0.518	0.562	0.496	
$v2$-$c1$ (π/d)	0.848	0.826	–	–	0.649	–	–	–	
Sample B									
$v1$-$c1(0)$	0.267	0.280	0.252						0.243
$v2$-$c1(0)$	0.399	0.346	0.363						0.351
$v3$-$c1(0)$	0.564	0.495	0.475						0.436
$v2$-$c1$ (π/d)	0.597	0.620	–						–
$v4$-$c1(0)$	0.719	0.706	–						–

reduces the power of the reflected light below the sensitivity limit of the experimental setup.

The same set of measurements was performed on sample B. In this case, the fundamental transition $v1$-$c1(0)$ is also nearly polarization independent. Here, $v2$-$c1(0)$, $v3$-$c1(0)$, and $v2$-$c1(\pi/d)$ are visible only for certain polarizer positions due to their low oscillator strength. The polarization dependence of $v2$-$c1(0)$ is contrary to $v3$-$c1(0)$ and $v2$-$c1(\pi/d)$. Here, $v4$-$c1(0)$ is evident at all polarizations.

IV. DISCUSSION

Our modeling predicted that bands $v2$ and $v3$ change their light/heavy hole character between 0 and π/d values of the SL wave vector. In sample A, transitions $v2$-$c1(0)$ and $v2$-$c1(\pi/d)$ have the opposite polarization dependence, despite originating from the same valence band. This supports the interchanging nature of $v2$ from light hole at $k_z = 0$ value to heavy hole at $k_z = \pi/d$. The sample B results are also consistent with this prediction, but it is not as clear as sample A. The sample B transitions $v2$-$c1(\pi/d)$ and $v3$-$c1$ have similar energies, in agreement with the calculations, leading their reflection features to blend. Therefore, their polarization properties are not clearly distinguishable from one another. The two blending features appear to have the same polarization dependence and, therefore, a common heavy hole character. This supports an interchange in the nature of $v2$.

We conclude that the gradient of valence nature (see Fig. 6) of the $v2$ band between $k_z = 0$ and π/d values was confirmed experimentally. Analyzing the calculations in Fig. 6, one can notice that the transitions related to the $v3$ band should also exhibit a similar behavior to the $v2$ transitions. Specifically, $v3$-$c1(0)$ should have a heavy hole nature and $v3$-$c1(\pi/d)$ a light hole nature. The experimental measurement of $v3$-$c1(0)$ agrees with this prediction. The $v3$-$c1(\pi/d)$ was not experimentally observed, and the theory does predict it has a low oscillator strength, so there is no polarization evidence related to it.

Several different modeling methods have been previously applied for band calculations of the InAs/GaSb SL material system. In Table III, the values obtained during the experiment have been compared with those predicted in previous studies.

Our numerical interface study of the system resulted in the observation that the ILA model, with the 0.6 nm bonding layer, is comparable with the RSA model, providing a similar energy ladder; however, the overlap integral for $v3$-$c1(0)$ does not seem accurate. Moreover, the value of the H_{XY}^{BA} parameter utilized within the RSA for the GaAs-like interface contributes weaker to the overall energy ladder than the H_{XY}^{AB} of the InSb-like interface. That agrees with the data presented in Refs. [51–53,70] regarding the mixed interface SL systems. Our final numerical model, fitted to the experimental data, assigns the values of H_{XY}^{AB} and H_{XY}^{BA} to 870 and 490 meV, respectively. These are consistent with Ref. [52]. However, in the literature, there is also a practice of zeroing the H_{XY}^{BA} parameter [52–54,70]. Following this approach, we also achieved fairly good agreement using the values of H_{XY}^{AB} between 500 and 600 meV.

V. CONCLUSIONS

In this paper, FTPL and FTPR studies of two InAs/GaSb SLs have been presented. A significant number of higher-order transitions have been observed in the measured PR spectra and analyzed vs temperature and probing light polarization. These observations allowed for the optimization of two numerical models (given in the eight $\mathbf{k}\cdot\mathbf{p}$ calculation formalism) to get a full energy ladder picture for the studied material structure.

Calculated valence band order at the boundary values of the k_z vector has been studied, and its light hole and heavy hole relations have been experimentally proven. For the two selected models, i.e., RSA and ILA, the numerical parameters have been given.

Finally, parametric values used in previous literature describing different models have been checked and reviewed in respect to our detected transitions and their not obvious analysis, i.e., the H_{XY} parameter utilized in the RSA model of the interface, and the optimal thickness of a single interface bonding layer for the ILA.

ACKNOWLEDGMENTS

The authors would like to thank Dr. Mateusz Dyksik, currently from Laboratoire National des Champs Magnétiques Intenses in Grenoble and Toulouse, France, for the fruitful discussion and tested spectra at the beginning of the study. This paper was supported by the Polish National Science Centre within Project No. 2014/15/B/ST7/04663, No. 2018/31/B/ST7/01541, and No. 2018/30/M/ST7/00174.

The authors have no competing interests to declare.

[1] M. W. Sigrist, *Air Monitoring by Spectroscopic Techniques* (Wiley, New York, 1994).

[2] D. M. Sonnenfroh, Interband cascade laser-based sensor for ambient CH_4, Opt. Eng. **49**, 111118 (2010).

[3] P. Kluczynski, S. Lundqvist, S. Belahsene, Y. Rouillard, L. Nähle, M. Fischer, and J. Koeth, Detection of propane using tunable diode laser spectroscopy at 3.37 μm, Appl. Phys. B **108**, 183 (2012).

[4] P. Kluczynski, M. Jahjah, L. Nähle, O. Axner, S. Belahsene, M. Fischer, J. Koeth, Y. Rouillard, J. Westberg, A. Vicet, and S. Lundqvist, Detection of acetylene impurities in ethylene and polyethylene manufacturing processes using tunable diode laser spectroscopy in the 3-μm range, Appl. Phys. B **105**, 427 (2011).

[5] S. Lundqvist, P. Kluczynski, R. Weih, M. von Edlinger, L. Nähle, M. Fischer, A. Bauer, S. Höfling, and J. Koeth, Sensing of formaldehyde using a distributed feedback interband cascade laser emitting around 3493 nm, Appl. Opt. **51**, 6009 (2012).

[6] F. K. Tittel, Current status of midinfrared quantum and interband cascade lasers for clinical breath analysis, Opt. Eng. **49**, 111123 (2010).

[7] C. Wang and P. Sahay, Breath analysis using laser spectroscopic techniques: breath biomarkers, spectral fingerprints, and detection limits, Sensors **9**, 8230 (2009).

[8] K. Vizbaras and M.-C. Amann, Room-temperature 3.73 μm GaSb-based type-I quantum-well lasers with quinternary barriers, Semicond. Sci. Technol. **27**, 032001 (2012).

[9] Q. Y. Lu, S. Manna, D. H. Wu, S. Slivken, and M. Razeghi, Shortwave quantum cascade laser frequency comb for multiheterodyne spectroscopy, Appl. Phys. Lett. **112**, 141104 (2018).

[10] I. Vurgaftman, W. W. Bewley, C. L. Canedy, C. S. Kim, M. Kim, C. D. Merritt, J. Abell, J. R. Lindle, and J. R. Meyer, Rebalancing of internally generated carriers for mid-infrared interband cascade lasers with very low power consumption, Nat. Commun. **2**, 585 (2011).

[11] C. Downs and T. Vandervelde, Progress in infrared photodetectors since 2000, Sensors **13**, 5054 (2013).

[12] P. Martyniuk, J. Antoszewski, M. Martyniuk, L. Faraone, and A. Rogalski, New concepts in infrared photodetector designs, Appl. Phys. Rev. **1**, 041102 (2014).

[13] M. Razeghi and B.-M. Nguyen, Advances in mid-infrared detection and imaging: a key issues review, Rep. Prog. Phys. **77**, 082401 (2014).

[14] M. Razeghi, S. Abdollahi Pour, E. Huang, G. Chen, A. Haddadi, and B. Nguyen, Type-II InAs/GaSb photodiodes and focal plane arrays aimed at high operating temperatures, OptoElectron. Rev. **19**, 261 (2011).

[15] A. Rogalski and P. Martyniuk, InAs/GaInSb superlattices as a promising material system for third generation infrared detectors, Infrared Phys. Technol. **48**, 39 (2006).

[16] E. A. Plis, InAs/GaSb type-II superlattice detectors, Adv. Electron. **2014**, 246769 (2014).

[17] A. Rogalski, P. Martyniuk, and M. Kopytko, InAs/GaSb type-II superlattice infrared detectors: future prospect, Appl. Phys. Rev. **4**, 031304 (2017).

[18] F. Szmulowicz, E. R. Heller, K. Fisher, and F. L. Madarasz, Optimization of absorption in InAs/$In_xGa_{1-x}Sb$ superlattices for long-wavelength infrared detection, Superlattices Microstruct. **17**, 373 (1995).

[19] B. M. Nguyen, Theoretical design and material growth of type-II antimonide-based superlattices for infrared detection and imaging, Ph.D. dissertation, Northwestern University, 2010.

[20] R. Müller, M. Haertelt, J. Niemasz, K. Schwarz, V. Daumer, Y. V. Flores, R. Ostendorf, and R. Rehm, Thermoelectrically-cooled InAs/GaSb type-II superlattice detectors as an alternative to HgCdTe in a real-time mid-infrared backscattering spectroscopy system, Micromachines **11**, 1124 (2020).

[21] J. Wróbel, L. Ciura, M. Motyka, F. Szmulowicz, A. Kolek, A. Kowalewski, P. Moszczyński, M. Dyksik, P. Madejczyk, S. Krishna, and A. Rogalski, Investigation of a near mid-gap trap energy level in mid-wavelength infrared InAs/GaSb type-II superlattices, Semicond. Sci. Technol. **30**, 115004 (2015).

[22] E. Gomółka, J. Rutkowski, P. Martyniuk, O. Markowska, M. Kopytko, A. Kowalewski, A. Rogalski, M. Motyka, and S. Krishna, Mid-wave InAs/GaSb superlattice barrier infrared detectors with NBnN and PBnN design, Bull. Pol. Acad. Sci.: Tech. Sci. **66**, 317 (2018).

[23] R. Kaspi, C. Moeller, A. Ongstad, M. L. Tilton, D. Gianardi, G. Dente, and P. Gopaladasu, Absorbance spectroscopy and identification of valence subband transitions in type-II InAs/GaSb superlattices, Appl. Phys. Lett. **76**, 409 (2000).

[24] A. P. Ongstad, R. Kaspi, C. E. Moeller, M. L. Tilton, D. M. Gianardi, J. R. Chavez, and G. C. Dente, Spectral blueshift and improved luminescent properties with increasing GaSb layer thickness in InAs-GaSb type-II superlattices, J. Appl. Phys. **89**, 2185 (2001).

[25] H. J. Haugan, K. Mahalingam, G. J. Brown, W. C. Mitchel, B. Ullrich, L. Grazulis, S. Elhamri, J. C. Wickett, and D. W. Stokes, Growth of short-period InAs/GaSb superlattices, J. Appl. Phys. **100**, 123110 (2006).

[26] B. Satpati, J. B. Rodriguez, A. Trampert, E. Tournié, A. Joullié, and P. Christol, Interface analysis of InAs/GaSb superlattice grown by MBE, J. Cryst. Growth **301–302**, 889 (2007).

[27] Y. Livneh, P. C. Klipstein, O. Klin, N. Snapi, S. Grossman, A. Glozman, and E. Weiss, $\mathbf{k} \cdot \mathbf{p}$ model for the energy dispersions and absorption spectra of InAs/GaSb type-II superlattices, Phys. Rev. B **86**, 235311 (2012).

[28] P. T. Webster, N. A. Riordan, S. Liu, E. H. Steenbergen, R. A. Synowicki, Y.-H. Zhang, and S. R. Johnson, Measurement of InAsSb bandgap energy and InAs/InAsSb band edge positions using spectroscopic ellipsometry and photoluminescence spectroscopy, J. Appl. Phys. **118**, 245706 (2015).

[29] X. Chen, L. Zhu, Y. Zhang, F. Zhang, S. Wang, and J. Shao, Modulated Photoluminescence InAs/GaSb Type-II Superlattice: In-Plane Optoelectronic Uniformity, Phys. Rev. Appl. **15**, 044007 (2021).

[30] N. Gautam, A. Barve, and S. Krishna, Identification of quantum confined interband transitions in type-II InAs/GaSb superlattices using polarization sensitive photocurrent spectroscopy, Appl. Phys. Lett. **101**, 221119 (2012).

[31] S. Alyamani, J. S. Kim, M. G. So, K. T. Hyeon, J. C. Shin, S. J. Lee, and J. O. Kim, Optical properties of InAs/GaSb multiple quantum wells by photoreflectance spectroscopy, in *2017 KPS Fall Meeting* (2017), http://kpsmeeting.kps.or.kr/sub07/view.html?num=1168.

[32] D. L. Smith and C. Mailhiot, Theory of semiconductor superlattice electronic structure, Rev. Mod. Phys. **62**, 173 (1990).

[33] J. Shen, S. Y. Ren, and J. D. Dow, Deep levels in type-II InAs/GaSb superlattices, Phys. Rev. B **46**, 6938 (1992).

[34] Y. Wei and M. Razeghi, Modeling of type-II InAs/GaSb superlattices using an empirical tight-binding method and interface engineering, Phys. Rev. B **69**, 085316 (2004).

[35] J. Wang and Y. Zhang, Band-gap corrected density functional theory calculations for InAs/GaSb type II superlattices, J. Appl. Phys. **116**, 214301 (2014).

[36] W.-F. Sun, M.-C. Li, and L.-C. Zhao, First-principles study of interface relaxation effect on interface and electronic structures of InAs/GaSb superlattices with different interface types, Superlattices Microstruct. **49**, 81 (2011).

[37] F. Bertazzi, A. Tibaldi, M. Goano, J. A. G. Montoya, and E. Bellotti, Nonequilibrium Green's Function Modeling of Type-II Superlattice Detectors and Its Connection to Semiclassical Approaches, Phys. Rev. Appl. **14**, 014083 (2020).

[38] G. C. Dente and M. L. Tilton, Pseudopotential methods for superlattices: applications to mid-infrared semiconductor lasers, J. Appl. Phys. **86**, 1420 (1999).

[39] G. C. Dente and M. L. Tilton, Comparing pseudopotential predictions for InAs/GaSb superlattices, Phys. Rev. B **66**, 165307 (2002).

[40] J.-M. Masur, R. Rehm, J. Schmitz, L. Kirste, and M. Walther, Four-component superlattice empirical pseudopotential method for InAs/GaSb superlattices, Infrared Phys. Technol. **61**, 129 (2013).

[41] L.-W. Wang, S.-H. Wei, T. Mattila, A. Zunger, I. Vurgaftman, and J. R. Meyer, Multiband coupling and electronic structure of $(InAs)_n/(GaSb)_n$ superlattices, Phys. Rev. B **60**, 5590 (1999).

[42] C. H. Grein, M. E. Flatté, J. T. Olesberg, S. A. Anson, L. Zhang, and T. F. Boggess, Auger recombination in narrow-gap semiconductor superlattices incorporating antimony, J. Appl. Phys. **92**, 7311 (2002).

[43] M. E. Flatté, and C. H. Grein, Theory and modeling of type-II strained-layer superlattice detectors, in *Quantum Sensing and Nanophotonic Devices VI*, edited by M. Razeghi, R. Sudharsanan, and G. J. Brown (SPIE, San Jose, 2009), Vol. 7222, p. 72220Q.

[44] M. E. Flatté, and C. E. Pryor, Defect states in type-II strained-layer superlattices, in *Quantum Sensing and Nanophotonic Devices VII*, edited by M. Razeghi, R. Sudharsanan, and G. J. Brown (SPIE, San Francisco, 2010), Vol. 7608, p. 760824.

[45] P.-F. Qiao, S. Mou, and S. L. Chuang, Electronic band structures and optical properties of type-II superlattice photodetectors with interfacial effect, Opt. Express **20**, 2319 (2012).

[46] I. Vurgaftman, G. Belenky, Y. Lin, D. Donetsky, L. Shterengas, G. Kipshidze, W. L. Sarney, and S. P. Svensson, Interband absorption strength in long-wave infrared type-II superlattices with small and large superlattice periods compared to bulk materials, Appl. Phys. Lett. **108**, 222101 (2016).

[47] P. C. Klipstein, Operator ordering and interface-band mixing in the Kane-like Hamiltonian of lattice-matched semiconductor superlattices with abrupt interfaces, Phys. Rev. B **81**, 235314 (2010).

[48] K. Ryczko, G. Sęk, and J. Misiewicz, Eight-band **k**·**p** modeling of InAs/InGaAsSb type-II W-design quantum well structures for interband cascade lasers emitting in a broad range of mid infrared, J. Appl. Phys. **114**, 223519 (2013).

[49] B. R. Bennett, B. V. Shanabrook, R. J. Wagner, J. L. Davis, J. R. Waterman, and M. E. Twigg, Interface composition control in InAs/GaSb superlattices, Solid State Electron. **37**, 733 (1994).

[50] W. H. Lau and M. E. Flatté, Effect of interface structure on the optical properties of InAs/GaSb laser active regions, Appl. Phys. Lett. **80**, 1683 (2002).

[51] L. L. Li, W. Xu, and F. M. Peeters, Intrinsic optical anisotropy of [001]-grown short-period InAs/GaSb superlattices, Phys. Rev. B **82**, 235422 (2010).

[52] F. Szmulowicz, H. Haugan, and G. J. Brown, Effect of interfaces and the spin-orbit band on the band gaps of InAs/GaSb superlattices beyond the standard envelope-function approximation, Phys. Rev. B **69**, 155321 (2004).

[53] E. Machowska-Podsiadlo and M. Bugajski, Eight-band **k**·**p** calculations of the electronic states in InAs/GaSb superlattices, in *2016 18th International Conference on Transparent Optical Networks (ICTON)* (IEEE, Piscataway, 2016), pp. 1–4.

[54] E. Machowska-Podsiadlo and M. Bugajski, Influence of various parameters and phenomena on the absorption edge of InAs/GaSb superlattices, Superlattices Microstruct. **125**, 214 (2019).

[55] R. Magri and A. Zunger, Effects of interfacial atomic segregation and intermixing on the electronic properties of InAs/GaSb superlattices, Phys. Rev. B **65**, 165302 (2002).

[56] A. Khoshakhlagh, F. Jaeckel, C. Hains, J. B. Rodriguez, L. R. Dawson, K. Malloy, and S. Krishna, Background carrier concentration in midwave and longwave InAs/GaSb type II superlattices on GaAs substrate, Appl. Phys. Lett. **97**, 051109 (2010).

[57] M. Motyka, G. Sęk, J. Misiewicz, A. Bauer, M. Dallner, S. Höfling, and A. Forchel, Fourier transformed photoreflectance and photoluminescence of mid infrared GaSb-based type II quantum wells, Appl. Phys. Express **2**, 126505 (2009).

[58] M. Motyka and J. Misiewicz, Fast differential reflectance spectroscopy of semiconductor structures for infrared applications by using Fourier transform spectrometer, Appl. Phys. Express **3**, 112401 (2010).

[59] M. Motyka, G. Sęk, F. Janiak, J. Misiewicz, K. Kłos, and J. Piotrowski, Fourier-transformed photoreflectance and fast differential reflectance of HgCdTe layers. The issues of spectral resolution and Fabry-Perot oscillations, Meas. Sci. Technol. **22**, 125601 (2011).

[60] E. L. Ivchenko, A. Y. Kaminski, and U. Rössler, Heavy-light hole mixing at zinc-blende (001) interfaces under normal incidence, Phys. Rev. B **54**, 5852 (1996).

[61] J. R. Waterman, B. V. Shanabrook, R. J. Wagner, M. J. Yang, J. L. Davis, and J. P. Omaggio, The effect of interface bond type

on the structural and optical properties of GaSb/InAs superlattices, Semicond. Sci. Technol. **8**, S106 (1993).

[62] I. Vurgaftman, J. R. Meyer, and L. R. Ram-Mohan, Band parameters for III-V compound semiconductors and their alloys, J. Appl. Phys. **89**, 5815 (2001).

[63] M. Motyka, G. Sęk, K. Ryczko, J. Misiewicz, T. Lehnhardt, S. Höfling, and A. Forchel, Optical properties of GaSb-based type II quantum wells as the active region of midinfrared interband cascade lasers for gas sensing applications, Appl. Phys. Lett. **94**, 251901 (2009).

[64] F. H. Pollak and H. Shen, Modulation spectroscopy of semiconductors: bulk/thin film, microstructures, surfaces/interfaces and devices, Mater. Sci. Eng. R Rep. **10**, xv (1993).

[65] D. E. Aspnes, Third-derivative modulation spectroscopy with low-field electroreflectance, Surf. Sci. **37**, 418 (1973).

[66] B. V. Shanabrook, O. J. Glembocki, and W. T. Beard, Photoreflectance modulation mechanisms in GaAs − $(Al)_x(Ga)_{1-x}As$ multiple quantum wells, Phys. Rev. B **35**, 2540(R) (1987).

[67] D. C. Larrabee, G. A. Khodaparast, J. Kono, K. Ueda, Y. Nakajima, M. Nakai, S. Sasa, M. Inoue, K. I. Kolokolov, J. Li, and C. Z. Ning, Temperature dependence of intersubband transitions in InAs/AlSb quantum wells, Appl. Phys. Lett. **83**, 3936 (2003).

[68] G. Bastard and J. Schulman, Wave mechanics applied to semiconductor heterostructures, Phys. Today **45**(2), 103 (1992).

[69] M. Motyka, M. Dyksik, K. Ryczko, R. Weih, M. Dallner, S. Höfling, M. Kamp, G. Sęk, and J. Misiewicz, Type-II quantum wells with tensile-strained GaAsSb layers for interband cascade lasers with tailored valence band mixing, Appl. Phys. Lett. **108**, 101905 (2016).

[70] H. M. Dong, L. L. Li, W. Xu, and K. Han, Effect of microscopic interface asymmetry on optical properties of short-period InAs/GaSb type-II superlattices, Thin Solid Films **589**, 388 (2015).